Electronic Supplementary Material (ESI) for Journal of Materials Chemistry A.

Supporting Information

A Tuned Lewis Acidic Catalyst Guided by Hard-soft Acid-base Theory to Promote N_2 Electroreduction

Yongwen Ren, Chang Yu,* Xuedan Song, Fengyi Zhou, Xinyi Tan, Yiwang Ding, Qianbing Wei, Jiafu Hong and Jieshan Qiu*

State Key Laboratory of Fine Chemicals, Liaoning Key Lab for Energy Materials and Chemical Engineering, School of Chemical Engineering, Dalian University of Technology, Dalian 116024, China

Corresponding Author

*E-mail: chang.yu@dlut.edu.cn (C.Y.).

*E-mail: jqiu@dlut.edu.cn (J.Q.).

Table of Contents 1. Experimental Procedures 2. Supporting Figures 3. Supporting Tables References

1. Experimental Procedures

1.1. Synthesis of MoS_x/CNTs

At first, the multiwalled carbon nanotubes (CNTs) were first oxidized by a plasma system (PCE-6 PLASMA CLEANER) for 10 min with a power of 19.6 W and a pressure of 50 Pa in oxygen atmosphere.[1] Subsequently, 12 mg of oxidized CNTs were dispersed in 20 mL of deionized (DI) water under ultrasonic conditions, and then transferred to a 250-mL beaker. After that, 1 mmol of ammonium tetrathiomolybdate ($(NH_4)_2MoS_4$) dissolved in 40 mL of DI water was added into the beaker, followed by adjusting the solution pH to ~3 using 1 M HCl.[2, 3] The mixed solution was further aged for 2 h with continuous stirring. Then the solid products were obtained by centrifugation, washed with DI water and anhydrous ethanol for several times, and lyophilized. Finally, it was annealed at 200 °C for 2 h with a heating rate of 2 °C min^{-1} in Ar atmosphere, yielding MoS_x/CNTs. For comparison, the pure MoS_x was also prepared by the same method above without the addition of CNTs.

1.2. Synthesis of MoS_x-O_{10}/CNTs, MoS_x-O_{30}/CNTs, MoS_x-O_{60}/CNTs, and MoS_x-O_{90}/CNTs

The as-obtained MoS_x/CNTs was directly heated at 200 °C for 10, 30, 60, and 90 min in air atmosphere and then cooled to room temperature, yielding MoS_x-O_{10}/CNTs, MoS_x-O_{30}/CNTs, MoS_x-O_{60}/CNTs, and MoS_x-O_{90}/CNTs, respectively.

1.3. Synthesis of MoS_x-P/CNTs

The MoS_x-P/CNTs was prepared through a simple thermal phosphorization method.[4] In a typical run, the MoS_x/CNTs and sodium hypophosphite ($NaH_2PO_2 \cdot H_2O$) were firstly mixed by grinding with the mass ratio of 1:2. Then the mixture was transferred into a quartz boat placed in the tube furnace and heated to 200 °C for 2 h with a heating rate of 2 °C min^{-1} in Ar atmosphere. The final MoS_x-P/CNTs was obtained by washing with excessive DI water and dried under vacuum at 60 °C for 8 h.

1.4. Characterization

The morphologies of the as-obtained catalysts were investigated by using scanning electron microscopy (SEM, QUANTA 450, 20 kV) equipped with element energy dispersive X-ray spectrometer (EDS) mapping, transmission electron microscopy (TEM, Tecnai G220), and high resolution transmission electron microscopy (HRTEM, FEI TF30). The weight ratio of CNTs in the catalyst was evaluated by thermogravimetric analysis (TGA, STA 449 F3) in a range of room temperature to 700 °C with a heating rate of 10 °C min^{-1} in air. The structure of the catalysts was examined with X-ray diffraction (XRD, D/MAX-2400) using Cu Kα radiation ($\lambda = 1.5406$ Å) and Raman spectroscopy (LabRAM HR Evolution, excited by 532 nm laser). The chemical compositions and the chemical states of molybdenum, sulfur, and oxygen for the samples were investigated by X-ray photoelectron spectroscopy (XPS, Thermo ESCALAB 250) with Al Kα X-ray radiation. The binding energies of XPS spectra were corrected for specimen charging by referencing C 1s to 284.6 eV. The curves of temperature-programmed desorption of N_2 (N_2-TPD) for the samples were collected with Micromeritics Auto Chem II 2920 analyzer. In particular, 100.0 mg of the sample was firstly preheated to 200 °C and kept for 30 min under Ar atmosphere, followed by cooling to 60 °C. Then the adsorption process of N_2 gas on the sample was performed in a N_2 gas atmosphere for 30 min with a flow rate of 30 mL min^{-1}. After 30 mL min^{-1} of Ar gas sweeping for 60 min, the samples were heated to 200 °C with a heating rate of 10 °C min^{-1} and the N_2-TPD curves were synchronously recorded by a thermal conductivity detector.

1.5. Cathode preparation

Typically, a homogeneous ink of catalyst was prepared by dispersing 4 mg catalyst into the mixed solution of 760 μL of anhydrous ethanol, 200 μL of deionized water, and 40 μL of Nafion solution (Alfa Aesar, 5 wt%) with the sonication assistance of 30 min. Then, the catalyst ink was dropped onto a carbon paper with a size of 1 × 1 cm^2 and dried at room temperature. The mass loading was calculated to be 0.1 mg cm^{-2}.

1.6. Electrochemical NRR measurements

The electrochemical measurements were conducted in a standard three electrode system controlled by a CHI 760 E electrochemistry workstation, in which Pt foil (1 × 1 cm^2) and Hg/HgO (1 M KOH) electrode were used as the counter and reference electrodes, respectively. All the potentials reported in this work were converted to the values versus reversible hydrogen electrode (*vs* RHE) scale by $E(\mathrm{RHE}) = E(\mathrm{Hg/HgO}) + 0.098 + 0.0591 \times \mathrm{pH}$. The N_2 before being used was purified by an alkaline solution (1 M KOH aqueous solution) and acidic solution cells (1 M H_2SO_4 aqueous solution) in sequence to remove any N-containing contamination.[5] The cathode cell filled with 30 mL of 0.1 M KOH electrolyte (pH = 13) was purged with purified N_2 for 30 min before the measurement, and then the electrochemical NRR was carried out with continuous feeding of N_2 at ambient temperature and pressure. Linear sweep voltammetry (LSV) was conducted at a scan rate of 5 mV s^{-1}. Constant potential electrolysis without *iR*-compensation was performed for 2 h at the potentials of −0.05, −0.10, −0.15, −0.20, −0.25 V *vs* RHE, respectively. For comparison, this test was also conducted by using Ar to replace the N_2. For better reproducibility, all the electrochemical experiments were repeated for three times to obtain the averaged values.

1.7. Determination of ammonia

The ammonia concentration was determined by Nessler reagent method and further confirmed by indophenol blue method.[6, 7] As for the Nessler reagent method, the Nessler reagent that consists of mercury (II) iodide and potassium iodide (KI) in an alkaline solution can interact with ammonia and form a colored complex ($HgO{\cdot}Hg(NH_2)I$) as follows.[8]

$$K_2HgI_4 + NH_3 + KOH \rightarrow HgO{\cdot}Hg(NH_2)I\downarrow + KI + H_2O \quad (1)$$

Therefore, the concentration of ammonia in the solution can be determined via the Ultraviolet-visible (UV-Vis) spectrophotometer at wavelengths between 410 and 425 nm. In the present work, we chose the absorbance values at the wavelength of 420 nm to construct the standard curve of Nessler reagent method and to measure the unknown concentrations of ammonia in the electrolytes on the basis of literature.[9, 10] Specifically, 2 mL of after-reaction electrolyte was taken from the cathode cell, followed by adding 2 mL of 1 M KOH solution and 1 mL of 0.2 M potassium sodium tartrate ($KNaC_4H_4O_6$) solution. Next, 0.5 mL of Nessler reagent was added into above solution and aged for 1 h at 25 °C. Subsequently, the absorbance of above solution was measured by an UV-Vis spectrophotometer at a wavelength of 420 nm. The standard curve was constructed by fitting the ammonia concentrations of reference solutions (0, 0.2, 0.4, 0.6, 0.8, 1.0, 1.5, and 2.0 μg mL^{-1}) versus corresponding absorbance value at 420 nm. The obtained fitting curve ($y = 0.151x + 0.021$, $R^2 = 0.9996$) exhibited a good linear relation and was employed to determine the unknown ammonia concentration of the electrolyte. The averaged ammonia concentrations at different potentials were obtained by measuring the corresponding electrolytes from the repeated constant potential electrolysis tests.

As for the indophenol blue method, the hypochlorite and phenol can react with ammonia and give the blue colored indophenol in an alkaline medium as follows.[8]

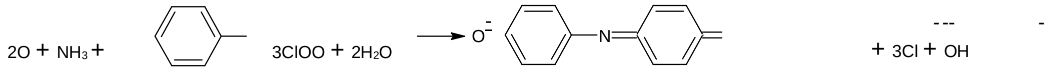

(2)

Therefore, the concentration of ammonia in the solution can be quantitatively determined via the UV-Vis spectrophotometer at wavelengths between 600 and 700 nm. In the present work, we chose the absorbance values at the wavelength of 655 nm to construct the standard curve of indophenol blue method and to measure the unknown concentrations of ammonia in the electrolytes on the basis of literature.[11, 12] In a typical run, 2 mL of 1 M NaOH solution containing 5% salicylic acid and 5% sodium citrate was added into 2 mL of electrolyte, followed by adding 1 mL of 0.05 M NaClO and 0.2 mL of 1% $C_5FeN_6Na_2O{\cdot}2H_2O$. After aging for 2 h at 25 °C, the absorbance of above solution was measured by a UV-Vis spectrophotometer at a wavelength of 655 nm. The standard curve was performed by fitting the ammonia concentrations of reference solutions (0, 0.2, 0.4, 0.6, 0.8, 1.0, 1.5, and 2.0 μg mL^{-1}) versus corresponding absorbance value at 655 nm. The fitting curve ($y = 0.41x + 0.031$, $R^2 = 0.9994$) showed a good linear relation and was used to measure the unknown ammonia concentration of electrolyte.

In order to identify the source of ammonia, the isotopic labeling experiment was conducted using $^{15}N_2$ (98 atom % ^{15}N) enriched gas as a feeding gas.[13] Specifically, the Ar gas was firstly purged through the electrolyte of cathode cell for 60 min to remove any $^{14}N_2$. Then the $^{15}N_2$ gas purified by the alkaline solution and acidic solution cells in sequence was purged for 15 min with a flow rate of 10 mL min^{-1}. After that, the constant potential electrolysis was conducted at −0.15 V *vs* RHE for 2 h in 0.1 M KOH in a circulation setup. The after-electrolysis electrolyte was taken out, and its pH value was adjusted to ~3 by 1 M HCl solution. Next, the water of the mixed solution was entirely removed by rotary evaporation, followed by adding 0.5 mL of d_6-dimethyl sulphoxide (d_6-DMSO). Finally, the d_6-DMSO containing $^{15}NH_4^+$ was characterized by ^1H nuclear magnetic resonance (^1H-NMR). The standard curve was constructed by fitting the $^{15}NH_4^+$ concentrations of reference solutions (0.1, 0.2, 0.3, 0.4, and 0.5 μg mL^{-1}) versus the integration areas of the peaks. The corresponding fitting curve ($y = 1.73x – 0.02$, $R^2 = 0.93$) showed a relatively good linear relation and was used to measure the unknown concentration of ammonia.

1.8. Determination of hydrazine

The concentration of hydrazine was determined by the Watt and Chrisp method.[14, 15] In brief, a color reagent was prepared by dissolving 5.99 g of *p*-dimethylaminobenzaldehyde (*p*-$C_9H_{11}NO$) in the mixed solution of 30 mL HCl and 300 mL ethanol. 5 mL of the color reagent was added into 5 mL of testing electrolyte. After aging for 20 min at 25 °C, the absorbance of above solution was measured by a UV-Vis spectrophotometer at a wavelength of 455 nm. The standard curve was obtained by fitting the hydrazine monohydrate ($N_2H_4 \cdot H_2O$) solutions with different concentrations (0, 0.1, 0.2, 0.4, 0.6, 0.8, and 1.0 μg mL^{-1}) versus corresponding absorbance value at 455 nm. The fitting curve showed a good linear relation of absorbance with $N_2H_4 \cdot H_2O$ concentration ($y = 1.021x + 0.075$, $R^2 = 0.9999$).

1.9. Calculation of NRR Faradaic efficiency and NH_3 yield rate

The Faradaic efficiency (FE) and mass-normalized yield rate of NH_3 were calculated as following:[6]

$$\mathrm{FE} = (3F \times C \times V)/17Q \tag{3}$$

$$\text{Yield rate} = (C \times V)/(t \times m) \tag{4}$$

where F is the Faraday constant (96,485 C mol^{-1}), C is the concentration of ammonia, V is the volume of the electrolyte (30 mL), Q is the total charge passed through the electrode, t is the electrolysis time (2 h), and m is the loading mass of the catalysts (0.1 mg).

1.10. Time-resolved *in situ* ATR-FTIR electrochemical measurements The ATR-FTIR experiments were carried out through a Bruker INVENIO-R spectrometer equipped with liquid nitrogen cooled mercury cadmium telluride (MCT) detector, a Veemax III ATR accessory (Kromatek), and a spectro-electrochemical cell. A Teflon cell was mounted onto a single bounce 60° CaF_2 crystal. The electrochemical measurements were performed with a three electrode system controlled by a CHI 760 E electrochemistry workstation, in which the Ag/AgCl (saturated KCl electrolyte) electrode and coiled Pt wire were used as the reference and counter electrodes, respectively. 10 μL of the catalyst ink was dropped on a Pt/C electrode with a geometric area of 0.28 cm^2, obtaining the working electrode. The mass loading of catalyst on Pt/C electrode was calculated to be 0.14 mg cm^{-2}. The N_2 inlet and gas outlet were connected on both sides of the cell.

Before tests, the purified N_2 was continuously purged into the 0.1 M KOH electrolyte in spectro-electrochemical cell for 30 min with a flow rate of 20 mL min^{-1}. After that the flow rate of N_2 was changed to 10 mL min^{-1}. Subsequently, a background spectrum was firstly collected, and the following spectra were performed by employing this background. Then the potentiostatic test was conducted at an applied potential of –0.15 V *vs* RHE with 100% *iR*-compensation. Synchronously, the *in situ* ATR-FTIR measurement was triggered with a resolution of 16 cm^{-1} in the range 1000−2500 cm^{-1} without atmospheric compensation, and corresponding spectra were recorded by the OPUS software.

1.11. Computational details

We carried out the first-principle density functional theory (DFT) calculations to investigate the electronic structures of the MoS_x catalysts and gain an insightful understanding for the mechanism of N_2 activation over MoS_x catalysts at an atom scale as implemented in the Vienna Ab initio Simulation Package (VASP) code.[16] Generalized gradient approximation (GGA) with Perdew–Burke–Ernzerh functional was employed to describe the exchange–correlation interactions.[17] Projector augmented wave (PAW) method was used and the spin polarization was considered for all the calculations.[18] A grid of 3×3×3 K-points was generated in Brillouin zone. The plane-wave basis was set to 520 eV, and the convergence thresholds for energy and force during structure relaxation were 1×10^{-4} eV atom^{-1} and 0.05 eV Å^{-1}, respectively.

2. Supporting Figures

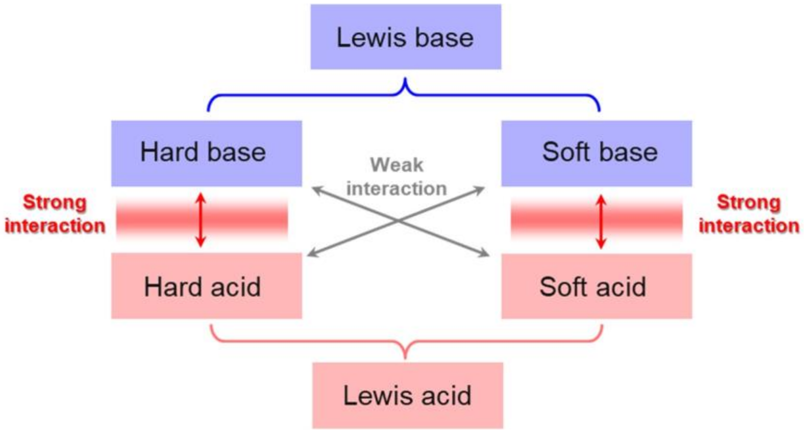

Fig. S1. Illustration for the HSAB theory. The HSAB theory developed by Pearson allows us to predict which the acids are preferrable to interact with the bases. In particular, the hard and soft base preferentially interact with the hard and soft acid, respectively. On the basis of this theory, we can construct the Lewis acid sites in the catalyst and regulate the corresponding acidity to match with the basicity of N_2 molecule (hard base), finally achieving an enhanced activation ability of catalyst toward N_2 molecule.

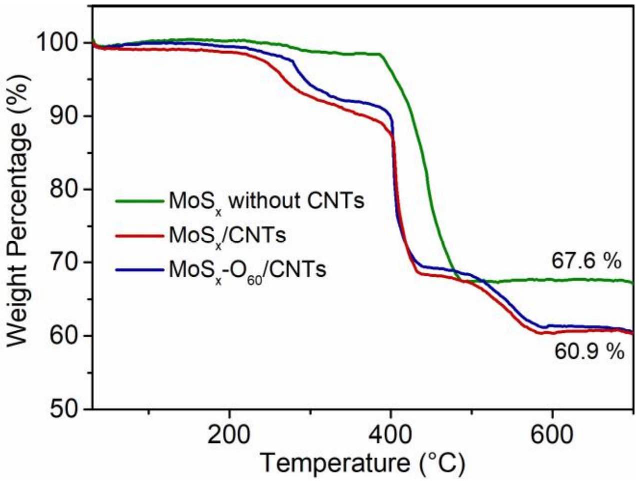

Fig. S2. TGA curves for the pure MoS_x without CNTs, MoS_x/CNTs, and MoS_x-O_{60}/CNTs. The TGA was performed in a range of room temperature to 700 °C with a heating rate of 10 °C min^{-1} in air atmosphere. The content of CNTs in MoS_x/CNTs and MoS_x-O_{60}/CNTs are calculated to be ~10 wt%.

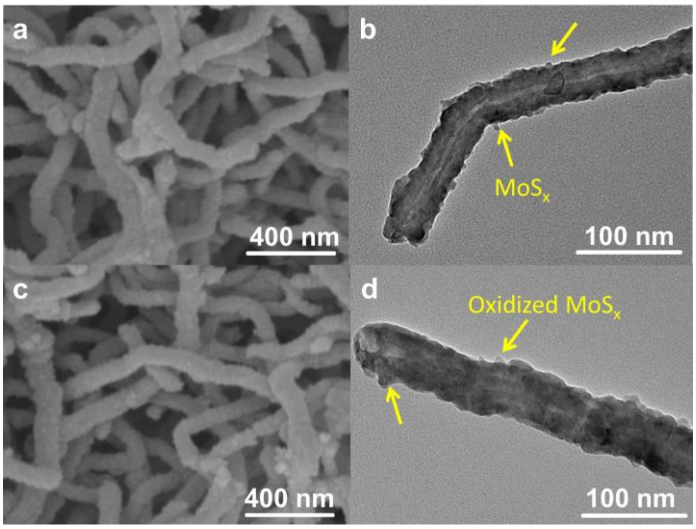

Fig. S3. SEM and TEM images for MoS$_x$/CNTs (a–b) and MoS$_x$-O$_{60}$/CNTs (c–d).

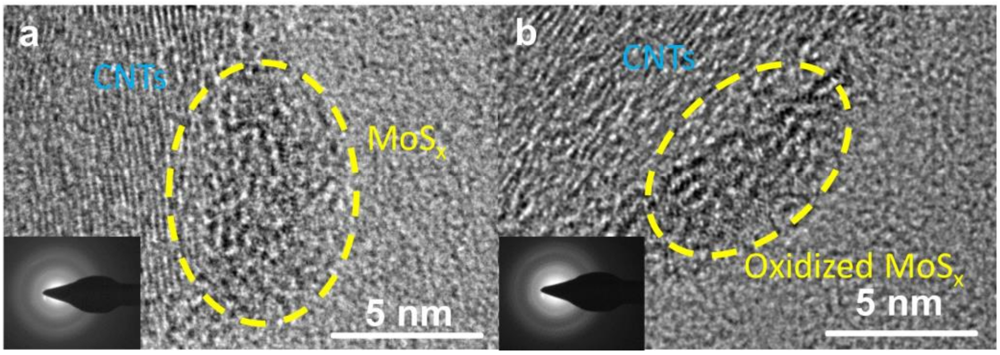

Fig. S4. HRTEM images of MoS$_x$/CNTs (a) and MoS$_x$-O$_{60}$/CNTs (b). The insets are corresponding SAED images.

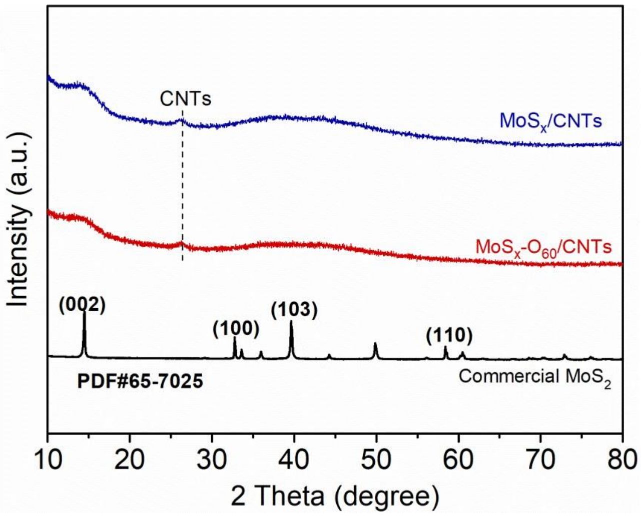

Fig. S5. XRD patterns of commercial MoS$_2$, MoS$_x$/CNTs, and MoS$_x$-O$_{60}$/CNTs.

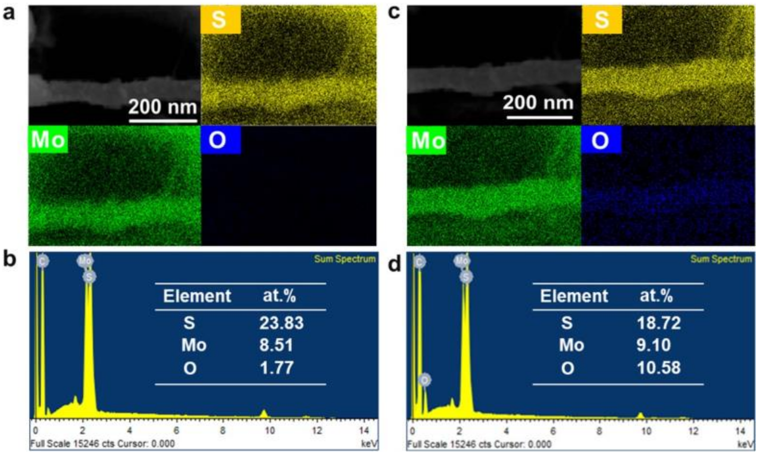

Fig. S6. SEM-EDS elemental mapping and corresponding EDX spectra for MoS_x/CNTs (a‒b) and MoS_x-O_{60}/CNTs (c‒d). It can be clearly seen that the O content of MoS_x-O_{60}/CNTs are much higher than that of MoS_x/CNTs, confirming the successful introduction of O element in MoS_x-O_{60}/CNTs via the oxidation treatment.

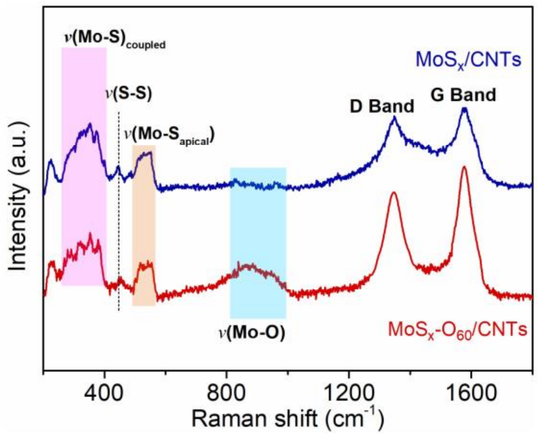

Fig. S7. Raman spectra of MoS_x/CNTs and MoS_x-O_{60}/CNTs.

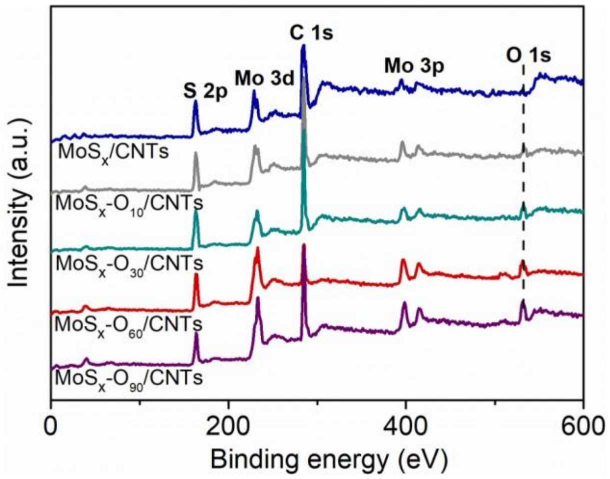

Fig. S8. XPS survey spectra of MoS_x/CNTs, MoS_x-O_{10}/CNTs, MoS_x-O_{30}/CNTs, MoS_x-O_{60}/CNTs, and MoS_x-O_{90}/CNTs.

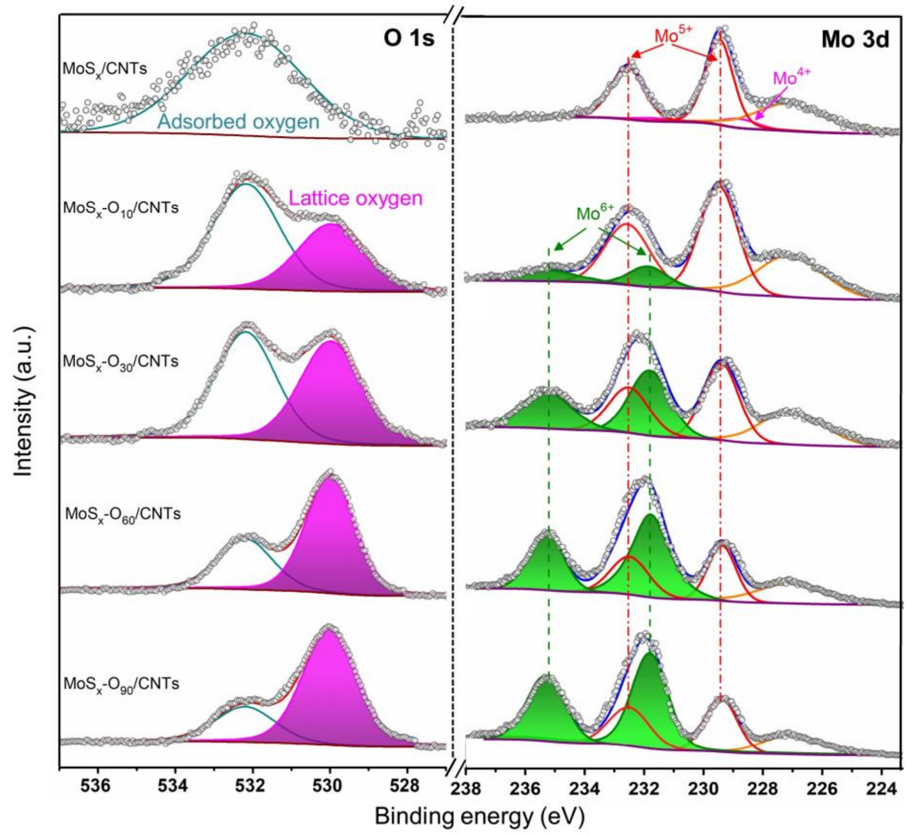

Fig. S9. High-resolution XPS spectra of O 1s and Mo 3d for MoS_x/CNTs, MoS_x-O_{10}/CNTs, MoS_x-O_{30}/CNTs, MoS_x-O_{60}/CNTs, and MoS_x-O_{90}/CNTs.

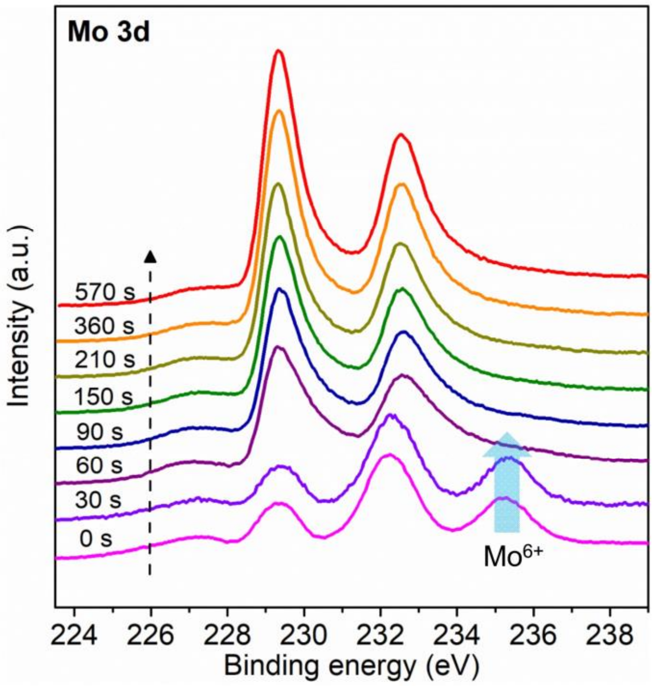

Fig. S10. The high-resolution Mo 3d XPS depth-profile spectra of MoS_x-O_{60}/CNTs after 0, 30, 60, 90, 150, 210, 360, and 570 s Ar ion etching.

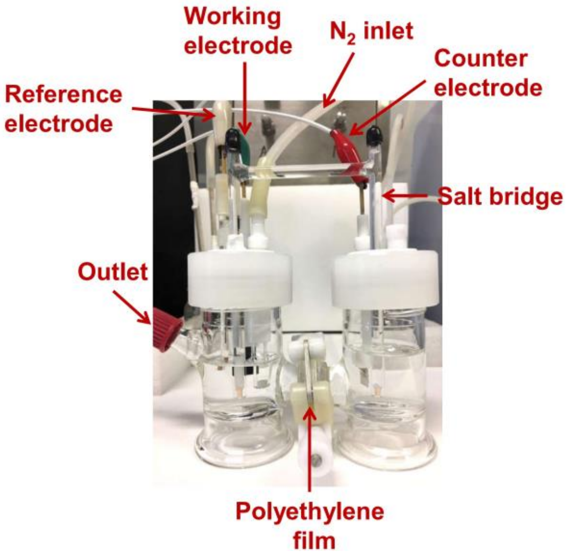

Fig. S11. Photograph of the electrocatalytic NRR device. The two chambers of the H-type cell were separated by a piece of polyethylene film with a thickness of 2 mm and connected by a salt bridge filled with saturation KCl solution.

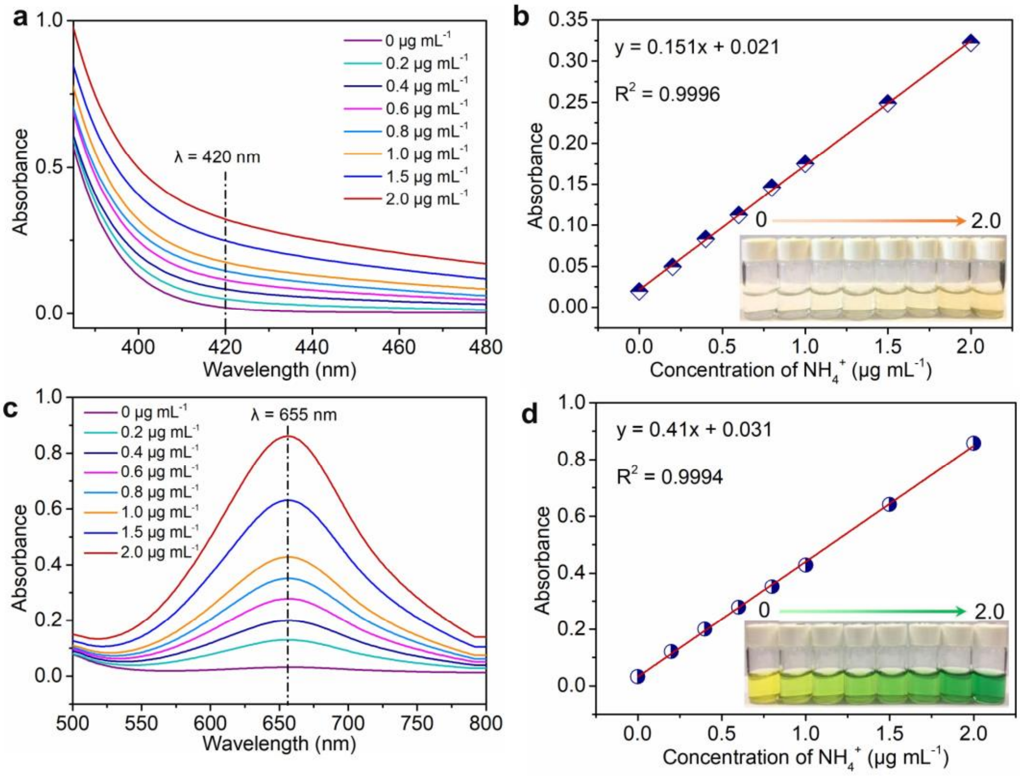

Fig. S12. (a−b) UV-Vis absorption spectra of standard solutions with different ammonia concentrations obtained by Nessler reagent method and corresponding calibration curve. The inset of (b) is the images of the standard solutions stained with Nessler reagent indicator. (c−d) UV-Vis absorption spectra of standard solutions with different ammonia concentrations determined by indophenol blue method and corresponding calibration curve. The inset of (d) is the images of the standard solutions stained with indophenol blue indicator.

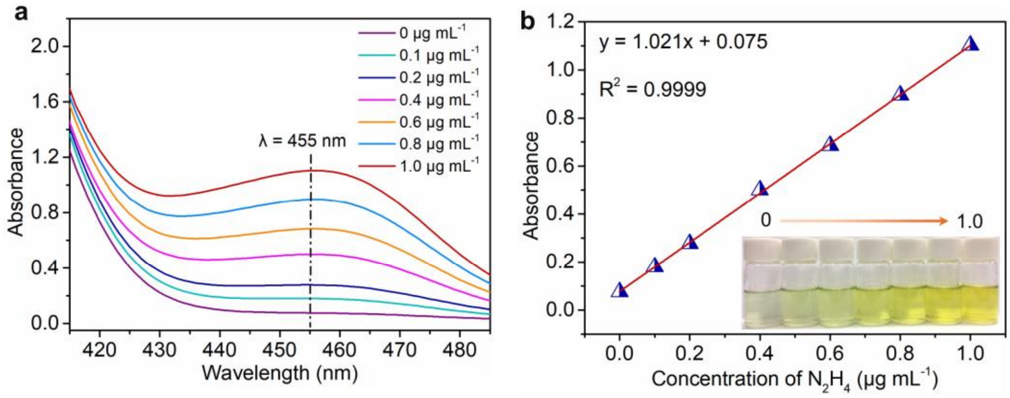

Fig. S13. (a−b) UV-Vis absorption spectra of standard solutions with different N_2H_4 concentrations determined by Watt and Chrisp method and corresponding calibration curve. The inset of (b) is the images of the standard solutions stained with Watt and Chrisp indicator.

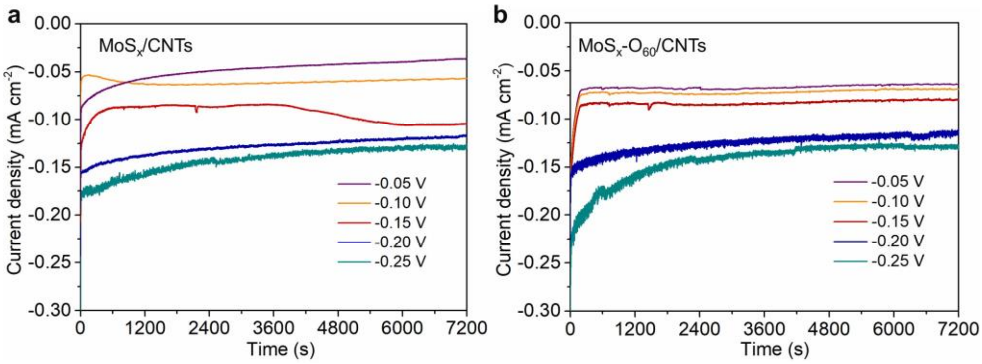

Fig. S14. The variations of current density versus time at various potentials in NRR process over MoS_x/CNTs (a) and MoS_x-O_{60}/CNTs (b).

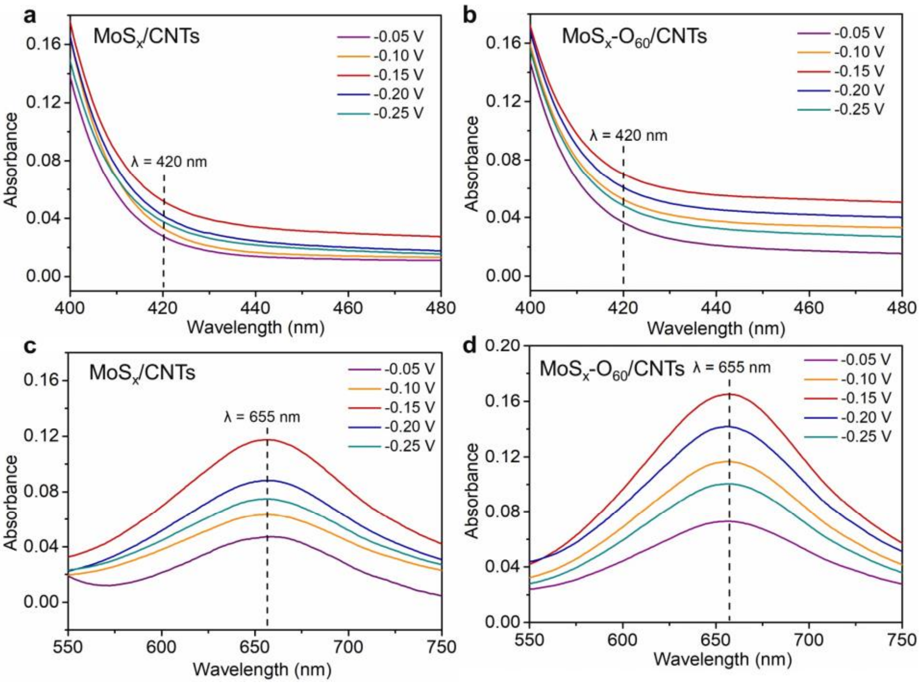

Fig. S15. UV-Vis absorption spectra of the electrolytes obtained with MoS$_x$/CNTs (a) and MoS$_x$-O$_{60}$/CNTs (b) as the electrocatalysts at various potentials stained with Nessler reagent indicator. UV-Vis absorption spectra of the electrolytes obtained using MoS$_x$/CNTs (c) and MoS$_x$-O$_{60}$/CNTs (d) as the electrocatalysts at various potentials stained with indophenol blue indicator.

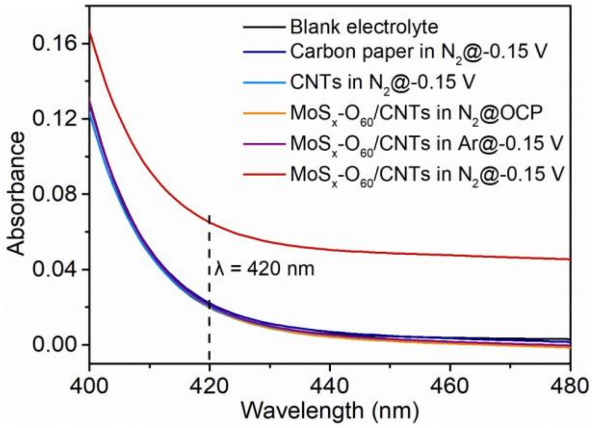

Fig. S16. UV-Vis absorption spectra of the blank electrolyte (0.1 M KOH), and the electrolytes obtained with carbon paper/CNTs as the electrocatalysts at −0.15 V under N$_2$ atmosphere, with MoS$_x$-O$_{60}$/CNTs as the electrocatalyst at open circuit potential (OCP) under N$_2$ atmosphere, with MoS$_x$-O$_{60}$/CNTs as the electrocatalyst at −0.15 V under Ar atmosphere, and with MoS_x-O_{60}/CNTs as the electrocatalyst at −0.15 V under N_2 atmosphere.

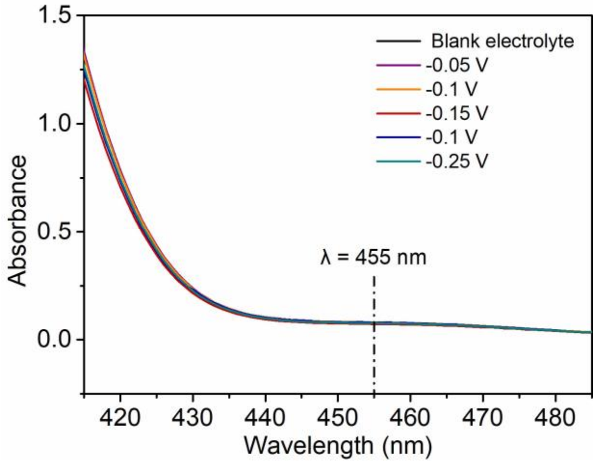

Fig. S17. UV-Vis absorption spectra of the blank electrolyte (0.1 M KOH) and the electrolytes obtained using MoS_x-O_{60}/CNTs as the electrocatalyst at various potentials under N_2 atmosphere.

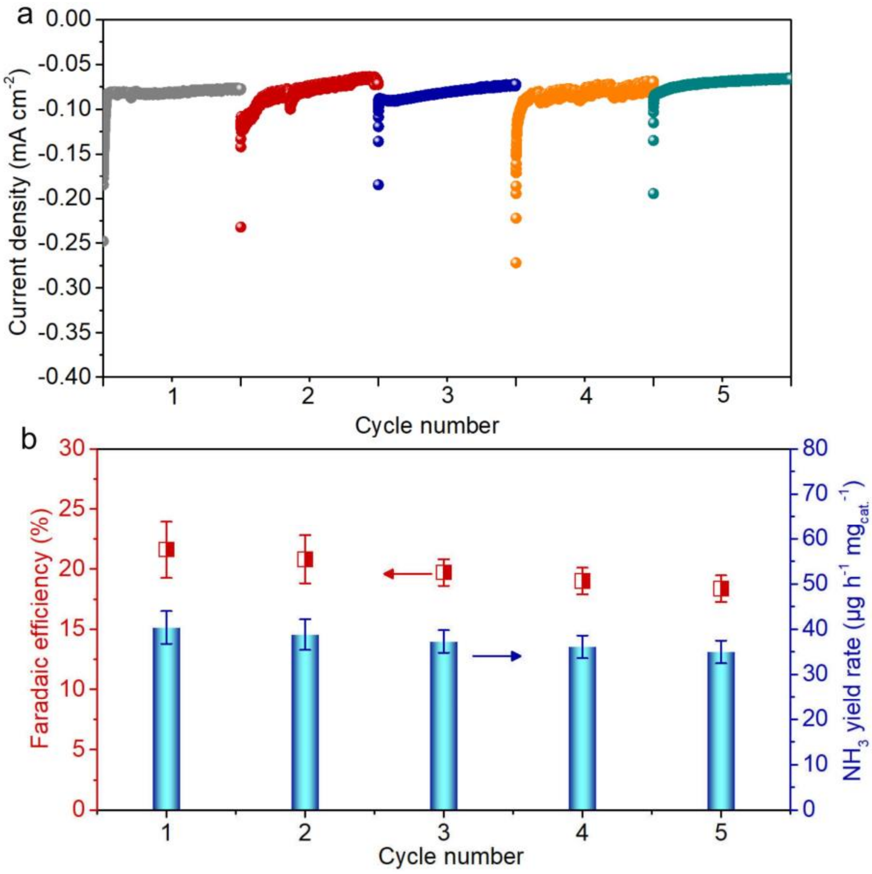

Fig. S18. (a) The current densities of NRR process by utilizing MoS_x-O_{60}/CNTs as the electrocatalyst during the consecutive cycling stability tests. Each cycle was conducted at −0.15 V for 2 h. (b) Corresponding FEs and NH_3 yield rates in the cycling stability tests.

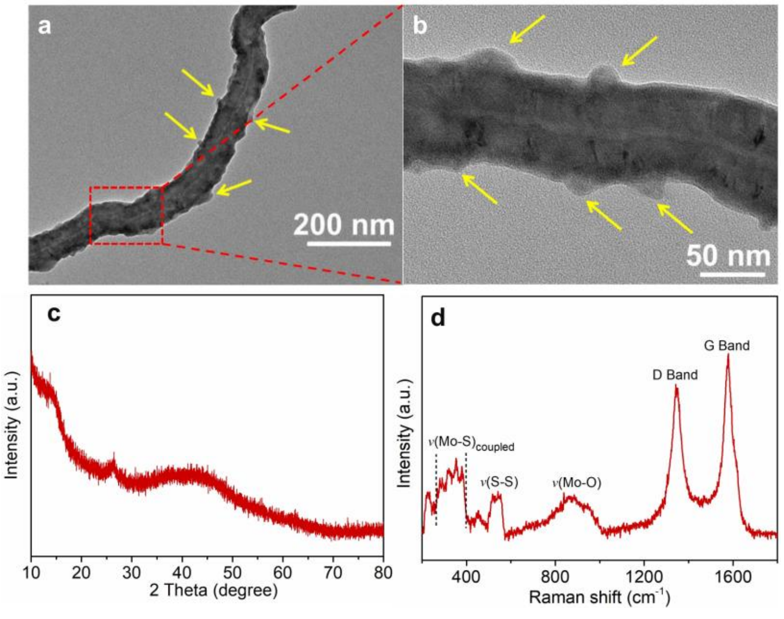

Fig. S19. The TEM images (a–b), XRD pattern (c), and Raman spectrum (d) of the MoS_x-O_{60}/CNTs after five continuous cycle tests at −0.15 V.

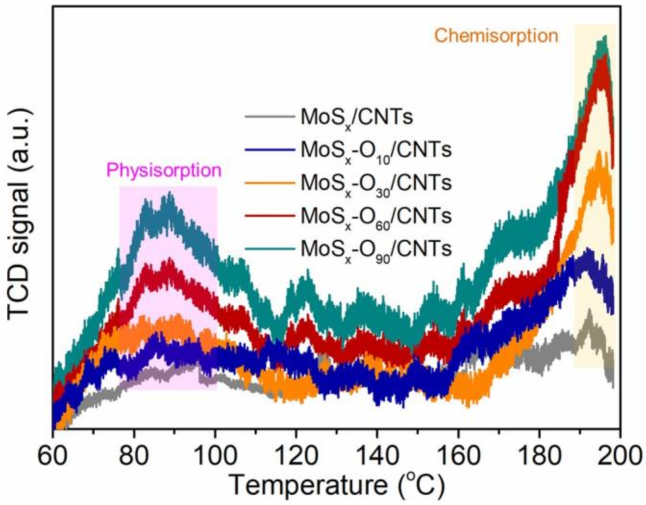

Fig. S20. N_2-TPD profiles of MoS$_x$/CNTs, MoS$_x$-O$_{10}$/CNTs, MoS$_x$-O$_{30}$/CNTs, MoS$_x$-O$_{60}$/CNTs, and MoS$_x$-O$_{90}$/CNTs. All the samples display two desorption peaks, where the peaks detected at ~90 °C and ~194 °C can be assigned to the physisorption and chemisorption of N_2 over the surface of as-made catalysts, respectively.[19, 20]

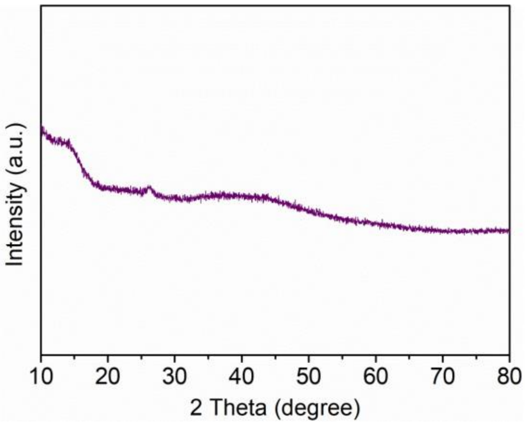

Fig. S21. XRD pattern of the MoS$_x$-P/CNTs.

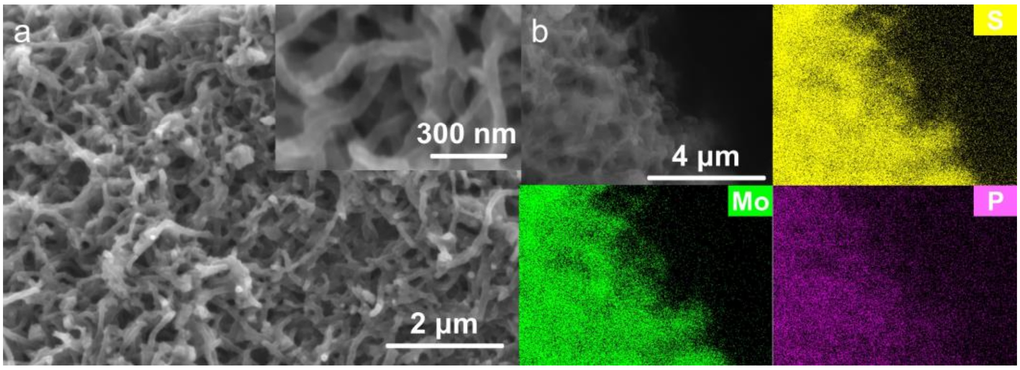

Fig. S22. (a−b) SEM image and SEM-EDS elemental mapping of the MoS$_x$-P/CNTs. The inset of (a) is the magnified SEM image of the MoS$_x$-P/CNTs.

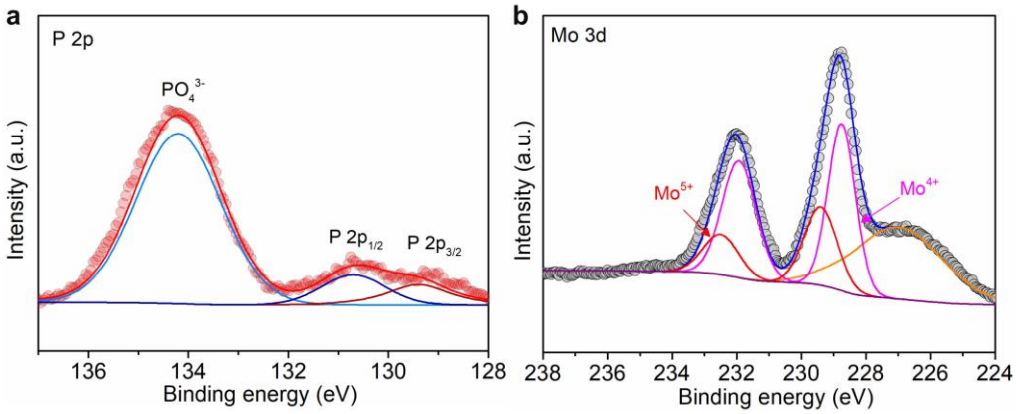

Fig. S23. High-resolution XPS spectra of P 2p (a) and Mo 3d (b) for MoS_x-P/CNTs. It should be noted that the predominant signal of PO_4^{3-} in P 2p spectrum is resulted from the oxidation of P, which can be effectively removed upon exposure to the aqueous electrolyte.[21] Therefore, it does not the NRR process.

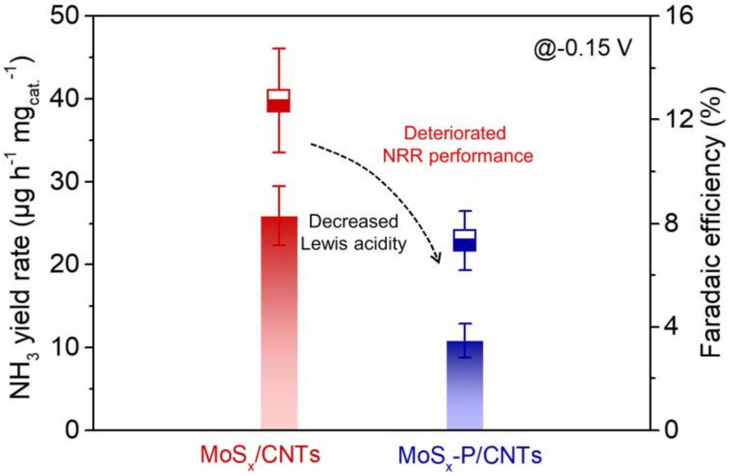

Fig. S24. Comparison of NRR performance for original MoS_x/CNTs and MoS_x-P/CNTs electrocatalysts at −0.15 V for 2 h under N_2 atmosphere.

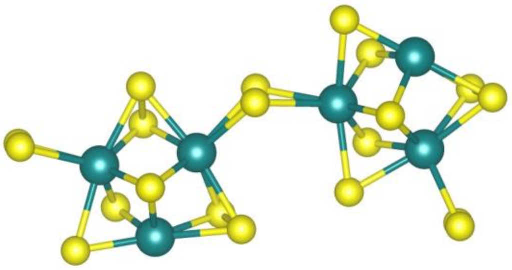

Fig. S25. The optimized structure model of MoS_x.

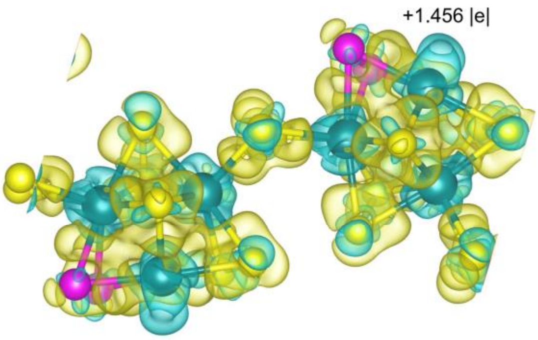

Fig. S26. The isosurface of deformation charge density for 2P-MoS_x and corresponding atomic charge of Mo (+1.456|e|) derived from Bader charge analysis. Light blue and light yellow regions represent charge loss and accumulation, respectively. Color scheme: dark green, Mo; yellow, S; pink, P. The isosurface is set to be 0.004 e/bohr^3.

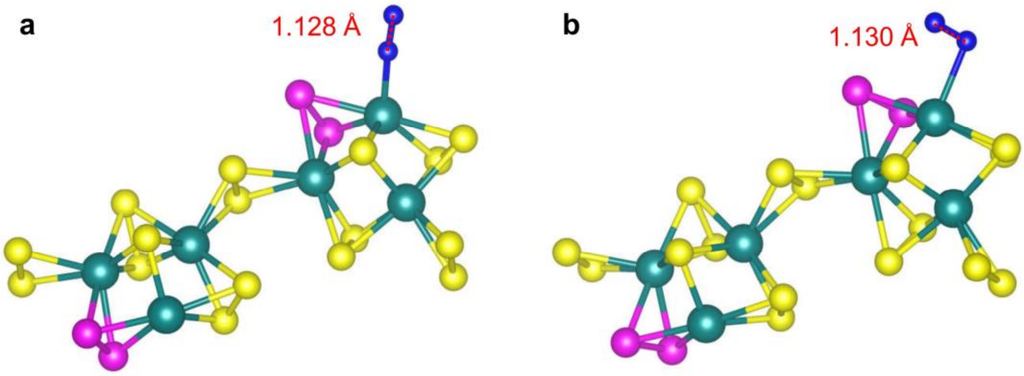

Fig. S27. The configurations and corresponding bond lengths of the adsorbed N_2 molecules in end-on (a) and side-on (b) modes over the Mo atoms of 2P-MoS_x. Color scheme: dark green, Mo; yellow, S; pink, P; blue, N.

3. Supporting Tables

Table S1. The relative content of Mo, S, and O elements in MoS_x samples and corresponding atomic ratios derived from XPS spectra.

Sample	Mo (at. %)	S (at. %)	O (at. %)	Mo: S: O
MoS_x/CNTs	11.02	30.25	2.87	1: 2.75: 0.26
MoS_x-O_{10}/CNTs	10.32	26.11	4.78	1: 2.53: 0.47
MoS_x-O_{30}/CNTs	11.83	27.04	7.83	1: 2.29: 0.66
MoS_x-O_{60}/CNTs	10.18	21.10	11.12	1: 1.97: 1.04

MoS_x-O_{90}/CNTs	10.96	20.80	12.51	1: 1.90: 1.14

Table S2. Comparison of the NRR performance for the as-made MoS_x-O_{60}/CNTs with reported Mo-based electrocatalysts in past three years at ambient conditions.

Publication year	Material	Electrolyte	FE (%)	NH_3 yield rate (μg_{-1} h_{-1} $mg_{cat.-1}$)	Quantitative $^{15}N_2$ test	Reference
–	**MoS_x-O_{60}/CNTs**	**0.1 M KOH**	**21.60 ± 2.35**	**40.4 ± 3.6**	**Yes**	***This work***
2020	Mo-doped FeS_2	0.1 M KOH	14.41	25.15	Yes	22
2020	Ru-doped Mo_2CT_X MXene	0.05 M K_2SO_4	25.77	40.57	Yes	23
2020	MoO_2 nanoparticles	0.1 M HCl	30	21.2	No	24
2020	Mo single atoms/Mo_2C nanoparticles	Mixture of 0.005 M H_2SO_4 and 0.1 M K_2SO_4	7.1	16.1	No	25
2020	MoN nanocrystals	0.1 M HCl	6.9	76.9	No	26
2020	PtMo alloy	0.1 M KOH	14.37	65.3	No	27
2019	Ru/MoS_2	0.01 M HCl	17.6	–	Yes	28
2018	MoO_3 nanosheets	0.1 M HCl	1.9	29.43	No	29
2018	MoS_2 nanosheets	0.1 M Na_2SO_4	8.34	29.28	No	30
2018	Mo_2C nanodots	0.5 M Li_2SO_4	7.8	11.3	No	31
2018	MoS_2 nanosheets	0.1 M Na_2SO_4	1.17	–	No	32

References

1. J. Hong, C. Yu, X. Song, X. Meng, H. Huang, C. Zhao, X. Han, Z. Wang and J. Qiu, *ACS Sustain. Chem. Eng.*, 2019, **7**, 7527–7534.
2. H. Ye, L. Wang, S. Deng, X. Zeng, K. Nie, P. N. Duchesne, B. Wang, S. Liu, J. Zhou, F. Zhao, N. Han, P. Zhang, J. Zhong, X. Sun, Y. Li, Y. Li and J. Lu, *Adv. Energy Mater.*, 2017, **7**, 1601602.
3. H. Ye, L. Ma, Y. Zhou, L. Wang, N. Han, F. Zhao, J. Deng, T. Wu, Y. Li and J. Lu, *Proc. Natl. Acad. Sci.*, 2017, **114**, 13091–13096.

4. X. Han, C. Yu, Y. Niu, Z. Wang, Y. Kang, Y. Ren, H. Wang, H. S. Park and J. Qiu, *Small Methods*, 2020, **4**, 2000546.
5. C.-C. Zhang, X. Liu, Y.-P. Liu and Y. Liu, *Chem. Mater.*, 2020, **32**, 8724– 8732.
6. L. Zhang, L. X. Ding, G. F. Chen, X. Yang and H. Wang, *Angew. Chem. Int. Ed.*, 2018, **58**, 2612–2616.
7. L. Zhang, M. Cong, X. Ding, Y. Jin, F. Xu, Y. Wang, L. Chen and L. Zhang, *Angew. Chem. Int. Ed.*, 2020, **59**, 10888−10893.
8. G. Qing, R. Ghazfar, S. T. Jackowski, F. Habibzadeh, M. M. Ashtiani, C. P. Chen, M. R. Smith and T. W. Hamann, *Chem. Rev.*, 2020, **120**, 5437–5516.
9. Y. Luo, G.-F. Chen, L. Ding, X. Chen, L.-X. Ding and H. Wang, *Joule*, 2019, **3**, 279–289.
10. Q. Qin, Y. Zhao, M. Schmallegger, T. Heil, J. Schmidt, R. Walczak, G. Gescheidt-Demner, H. Jiao and M. Oschatz, *Angew. Chem. Int. Ed.*, 2019, **58**, 13101–13106.
11. L. Li, C. Tang, D. Yao, Y. Zheng and S.-Z. Qiao, *ACS Energy Lett.*, 2019, **4**, 2111–2116.
12. B. Hu, M. Hu, L. Seefeldt and T. L. Liu, *ACS Energy Lett.*, 2019, **4**, 1053– 1054.
13. S. Z. Andersen, V. Čolić, S. Yang, J. A. Schwalbe, A. C. Nielander, J. M. McEnaney, K. Enemark-Rasmussen, J. G. Baker, A. R. Singh, B. A. Rohr, M. J. Statt, S. J. Blair, S. Mezzavilla, J. Kibsgaard, P. C. K. Vesborg, M. Cargnello, S. F. Bent, T. F. Jaramillo, I. E. L. Stephens, J. K. Nørskov and I. Chorkendorff, *Nature*, 2019, **570**, 504–508.
14. J. Li, S. Chen, F. Quan, G. Zhan, F. Jia, Z. Ai and L. Zhang, *Chem*, 2020, **6**, 885–901.
15. C. Lv, L. Zhong, Y. Yao, D. Liu, Y. Kong, X. Jin, Z. Fang, W. Xu, C. Yan, K. N. Dinh, M. Shao, L. Song, G. Chen, S. Li, Q. Yan and G. Yu, *Chem*, 2020, **6**, 2690–2702.
16. G. Kresse and J. Furthmüller, *Phys. Rev. B*, 1996, **56**, 11169−11186.
17. J. P. Perdew, K. Burke and M. Ernzerhof, *Phys. Rev. Lett.*, 1996, **77**, 3865−3868.
18. P. E. Blochl, *Phys. Rev. B*, 1994, **50**, 17953−17979.
19. P. Wang, Y. Ji, Q. Shao, Y. Li and X. Huang, *Sci. Bull.*, 2020, **65**, 350–358.
20. X. Yu, P. Han, Z. Wei, L. Huang, Z. Gu, S. Peng, J. Ma and G. Zheng, *Joule*, 2018, **2**, 1610–1622.
21. J. Liu, Z. Wang, J. Li, L. Cao, Z. Lu and D. Zhu, *Small*, 2020, **16**, 1905738.
22. H.-B. Wang, J.-Q. Wang, R. Zhang, C.-Q. Cheng, K.-W. Qiu, Y.-j. Yang, J. Mao, H. Liu, M. Du, C.-K. Dong and X.-W. Du, *ACS Catal.*, 2020, **10**, 4914–4921.
23. W. Peng, M. Luo, X. Xu, K. Jiang, M. Peng, D. Chen, T. S. Chan and Y. Tan, *Adv. Energy Mater.*, 2020, **10**, 2001364.
24. X. Han, C. S. Gerke, S. Banerjee, M. Zubair, J. Jiang, N. M. Bedford, E. M. Miller and V. S. Thoi, *ACS Energy Lett.*, 2020, **5**, 3237–3243.

25. Y. Ma, T. Yang, H. Zou, W. Zang, Z. Kou, L. Mao, Y. Feng, L. Shen, S. J. Pennycook, L. Duan, X. Li and J. Wang, *Adv. Mater.*, 2020, **32**, 2002177.
26. X. Yang, F. Ling, J. Su, X. Zi, H. Zhang, H. Zhang, J. Li, M. Zhou and Y. Wang, *Appl. Catal. B−Environ.*, 2020, **264**, 118477.
27. X. Guo, X. Li, Y. Li, J. Yang, X. Wan, L. Chen, J. Liu, X. Liu, R. Yu, L. Zheng and J. Shui, *Nano Energy*, 2020, **78**, 105211.
28. B. H. R. Suryanto, D. Wang, L. M. Azofra, M. Harb, L. Cavallo, R. Jalili, D. R. G. Mitchell, M. Chatti and D. R. MacFarlane, *ACS Energy Lett.*, 2019, **4**, 430−435.
29. J. Han, X. Ji, X. Ren, G. Cui, L. Li, F. Xie, H. Wang, B. Li and X. Sun, *J. Mater. Chem. A*, 2018, **6**, 12974–12977.
30. X. Li, T. Li, Y. Ma, Q. Wei, W. Qiu, H. Guo, X. Shi, P. Zhang, A. M. Asiri, L. Chen, B. Tang and X. Sun, *Adv. Energy Mater.*, 2018, **8**, 1801357.
31. H. Cheng, L. X. Ding, G. F. Chen, L. Zhang, J. Xue and H. Wang, *Adv. Mater.*, 2018, **30**, 1803694.
32. L. Zhang, X. Ji, X. Ren, Y. Ma, X. Shi, Z. Tian, A. M. Asiri, L. Chen, B. Tang and X. Sun, *Adv. Mater.*, 2018, **30**, 1800191.